A Flexible 2.45-GHz Power Harvesting Wristband With Net System Output From −24.3 dBm of RF Power

Salah-Eddine Adami, Plamen Proynov, Geoffrey S. Hilton, Guang Yang, Chunhong Zhang, Dibin Zhu, Yi Li, Steve P. Beeby, Ian J. Craddock, *Fellow, IEEE*, and Bernard H. Stark

***Abstract*— This paper presents a flexible 2.45-GHz wireless power harvesting wristband that generates a net dc output from a −24.3-dBm RF input. This is the lowest reported system sensitivity for systems comprising a rectenna and impedance-matching power management. A complete system has been implemented comprising: a fabric antenna, a rectifier on rigid substrate, a contactless electrical connection between rigid and flexible subsystems, and power electronics impedance matching. Various fabric and flexible materials are electrically characterized at 2.45 GHz using the two-line and the T-resonator methods. Selected materials are used to design an all-textile antenna, which demonstrates a radiation efficiency above 62% on a phantom irrespective of location, and a stable radiation pattern. The rectifier, designed on a rigid substrate, shows a best-in-class efficiency of 33.6% at −20 dBm. A reliable, efficient, and wideband contactless connection between the fabric antenna and the rectifier is created using broadside-coupled microstrip lines, with an insertion loss below 1 dB from 1.8 to over 10 GHz. A self-powered boost converter with a quiescent current of 150 nA matches the rectenna output with a matching efficiency above 95%. The maximum end-to-end efficiency is 28.7% at −7 dBm. The wristband harvester demonstrates net positive energy harvesting from −24.3 dBm, a 7.3-dB improvement on the state of the art.**

***Index Terms*— Boost converter, fabric antenna, fabric-to-PCB connector, Internet of Things, power management, rectenna array, rectenna impedance matching, rectennas, RF energy harvesting, RF power transfer, smart fabric, T-resonator method, textile antenna, two-line method.**

I. Introduction

FLEXIBLE RF electronics has many applications in on-body and off-body communications for: healthcare [1], RFID body-centric sensing [2], wearables [3], protective garments for firefighters [4], life jackets for Cospas-Sarsat international satellite rescue system [5], and spacesuits [6]. Flexible RF and microwave circuits have been reported using flexible thin polymers [7], fabric materials [8], [9], and inkjet-printed structures using paper [10]. Fabrics are particularly relevant for wearables due to their broad acceptance, flexibility, lightweight, and low cost. In practice, where high functionality is required, a hybrid structure is used, where flexible circuits are combined with rigid sub-PCBs with the required RF and sensor-node chipsets [11]. RF wireless power transfer provides a convenient means of remotely powering these hybrid structures [12], removing the need to directly recharge batteries. This arrangement furthermore avoids the need for rigid, dense, and potentially toxic batteries.

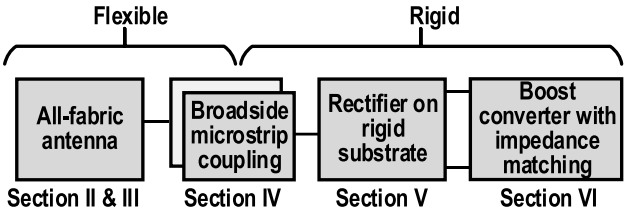

Fig. 1. Block diagram of the flexible RF power harvesting system (single channel).

The combination of RF wireless power transfer and wearable electronics is challenging for several reasons. First, the reliability of interconnections between flexible and rigid subsystems needs addressing, for example by using snap-on fasteners, as reported in [13]. Second, in order to maximize the output power, and obtain a range of several meters, rectification and power management circuits need to be efficient down to extremely low power levels [14]. Third, with the antenna being on a moving person, the stability of efficiency and radiation pattern is important.

This paper reports, for the first time, a flexible and wearable end-to-end RF-harvesting system, that is designed to operate over a range exceeding 2 m at Wi-Fi transmit power levels (100-mW EIRP). A single channel of this system is illustrated in Fig. 1. The flexible fabric antenna is coupled to the rigid rectifier and boost converter, using broadside-coupled microstrip lines. This system is optimized to operate at a power of −20 dBm in the center of the 2.4-GHz ISM band. This power level gives a good balance between transmission range (about 2 m from a 100-mW EIRP typical Wi-Fi source [15]) and available dc power for the load (about 1 μW, hence a 10%

Manuscript received November 28, 2016; revised March 6, 2017 and April 13, 2017; accepted April 16, 2017. This work was performed under the SPHERE Interdisciplinary Research Collaboration (IRC) funded by the U.K. Engineering and Physical Sciences Research Council (EPSRC), Grant EP/K031910/1. *(Corresponding author: Salah-Eddine Adami.)*

S.-E. Adami, P. Proynov, G. S. Hilton, G. Yang, I. J. Craddock, and B. H. Stark are with the Department of Electrical and Electronic Engineering, University of Bristol, Bristol BS8 1UB, U.K. (e-mail: bernard.stark@bristol.ac.uk).

C. Zhang was with the Department of Electrical and Electronic Engineering, University of Bristol, Bristol BS8 1UB, U.K.

D. Zhu is with the College of Engineering, Mathematics and Physical Sciences, University of Exeter, Exeter EX4 4QF, U.K. (e-mail: d.zhu@exeter.ac.uk).

Y. Li and S. P. Beeby are with the Department of Electronics and Computer Science, University of Southampton, Southampton SO17 1BJ, U.K. (e-mail: yi.li@soton.ac.uk; spb@ecs.soton.ac.uk).

Color versions of one or more of the figures in this paper are available online at http://ieeexplore.ieee.org.

Digital Object Identifier 10.1109/TMTT.2017.2700299

TABLE I
CHARACTERIZATION RESULTS OF VARIOUS SUBSTRATE MATERIALS AT THE 2.45-GHz BAND

Category	Candidate materials	h (mm)	Two-Line Method		T-resonator Method	α_{Typ} (dB/m) Typical Microstrip line, w=3 mm and h=1.6 mm	Suitable for screen printing
			ε_r	$tan\delta$	ε_r		
Sandwich used in [12]	Polycotton (1/3 of thick.) + standard Interface material (2/3 of thick.)	0.95	3.23	0.06	3.2	22.4	Good
Interface (Smart Fabric Inks Ltd.)	Standard interface material (Fabink-UV-IF1, used in [12])	1.94	3.26	0.063	3	23.6	Good
	Waterproof interface material (Fabink-UV-IF010)	1.4	2.68	0.052	2.75	17.9	Good
Felt (Fabric Land, UK)	Polyester felt	1.65	1.2	0.023	1.14	5.8	Poor
Woven (Fabric Land, UK)	Cotton woven	0.41	2	0.028	2.05	8.5	Acceptable
	Woven polyester	0.33	1.5	0.028	1.52	7.6	Acceptable
Polymers (DuPont™)	Flexible thin Kapton® polyimide film	1	2.8	0.014	2.83	4.9	Excellent
Reference	Duroid-5880 (Roger Corp.)	1.57	NPB	NPB	2.18	0.3	Excellent
	FR4 (Mega-electronics, UK)	1.6	4.22	0.017	4.2	7.6	Excellent

Legend: h: height of the substrate, **Suitable for screen printing,** from low to high: Poor-Acceptable-Good-Excellent, **NPH**: Non-Physical behaviour.

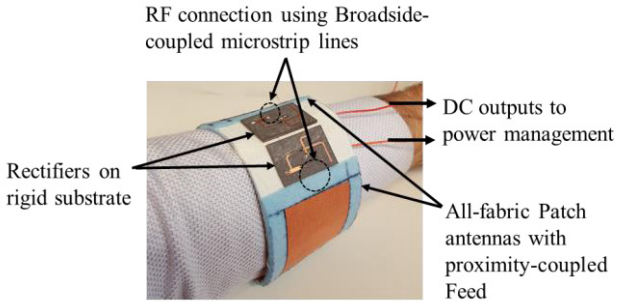

Fig. 2. Photograph of the proposed RF harvesting wristband system comprising two rectennas of that shown in Fig. 1.

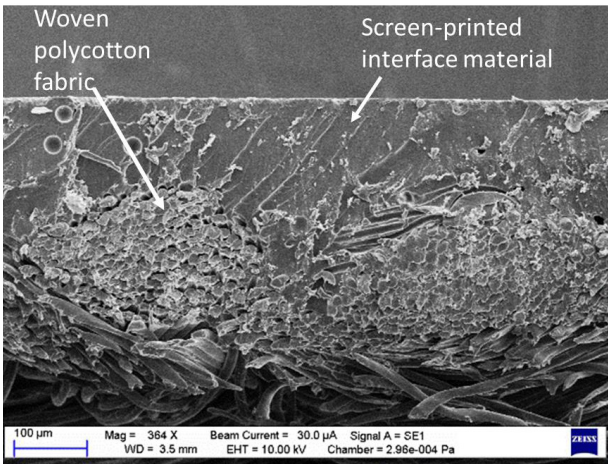

Fig. 3. Cross-sectional SEM image view of a standard polycotton fabric with screen-printed interface layer. The roughness of the fabric material is reduced to few micrometers.

end-to-end RF/dc efficiency). This system is implemented as a wristband, as shown in Fig. 2. This paper presents advances in various areas: antenna, rectifier, interconnection design, and power management. It validates the approach through both simulation and measurement of individual components and through experimental results from a complete system implementation.

The paper is organized as follows. Section II presents the characterization at 2.45 GHz of various materials. Section III presents the design of the fabric antenna. Section IV shows the design of the fabric-to-rigid PCB coupling interface. Section V presents the design of the rectifier. Section VI presents the power management circuit. Finally, in Section VII, the end-to-end system is presented along with experimental results.

II. CHARACTERIZATION OF TEXTILE MATERIALS AT 2.45 GHz

A. Characterization Method

The two-line method [16], [17] is used here to characterize various textile and other flexible materials, as shown in Table I, with FR4 and Duroid-5880 used as baselines. The selected materials cover a wide range of application areas with a focus on purely fabric materials. Foam materials were not considered here, although they were used in many other research papers to design fabric antennas [8]. Polyester and Cotton fabrics are at the top of our selection as they are widely used in garment industry. The list also includes an UV-curable polyurethane acrylate-based standard interface material (Fabink-UV-IF1) and a waterproof interface material (Fabink-UV-IF010), both from Smart Fabric Inks Ltd. These are used in [12], to planarise the surface of fabrics prior to the silver screen printing of antennas. Fig. 3 shows a cross-sectional scanning electron microscope (SEM) image of a polycotton fabric with screen-printed interface material. It can be seen that the rough surface of fabric is reduced to only few micrometers. Kapton polyimide laminate from DuPont is also characterized.

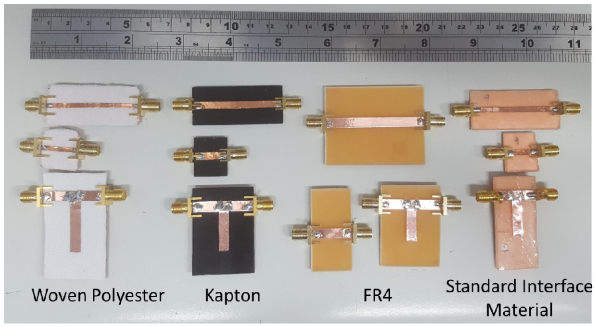

Fig. 4. Examples of samples characterized using the two-line and the T-resonator methods.

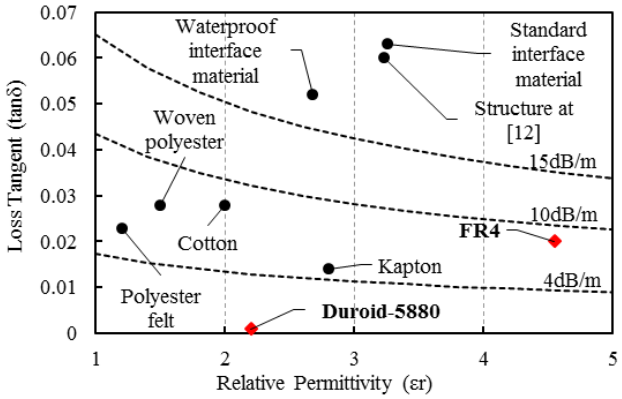

Fig. 5. Characterization results of various materials at 2.45 GHz: loss tangent versus relative permittivity. Contours of constant microstrip line dielectric loss are also plotted considering a typical microstrip line of width $w = 3$ mm over a $h = 1.6$ mm height substrate.

For each material, two microstrip lines of different lengths are produced (see Fig. 4). The relative permittivity ε_r and loss tangent tanδ are calculated from the measured S-parameters. Table I gives the results of the experimental characterization. The results of the characterization are also plotted in Fig. 5, with contours of constant dielectric attenuation.

The two-line method gives an estimation of the material characteristics for a relatively wide frequency range. However, the resulting tanδ can appear to be a nonmonotonic function of frequency [12], [17], as a consequence of multiple reflexions and standing waves in the relatively small samples under test. Nonphysical behavior can also appear when the two-line method is used on substrates with low dielectric loss (such as Duroid-5880). Averaging [17] or polynomial fitting [12] is normally required to smooth the final results. A second verification using a narrowband technique (e.g., antenna efficiency [18], T-resonator [19], ring resonator [20], resonant cavity, and cavity perturbation [21]) is recommended when an accurate characterization is required for a given frequency. As a validation in this paper, the T-resonator method is used to estimate the permittivity of the samples measured with the two-line method. T-resonator samples are designed to resonate around 2.45 GHz using the results from the two-line method (see Fig. 4). The results of the T-resonator characterization are summarized in Table I. One can see the excellent match with the results found using the two methods. Loss tangent was not extracted from the T-junction samples as a specific calibration kit need to be designed for each sample, which is quite impracticable considering the number of samples tested here. The extracted loss tangent of FR4 using the two-line method was 0.017 which is very similar to what was found in [19]. The other materials in our table have similar or even higher loss tangent than FR4. Therefore, loss tangent for those materials is estimated to have similar or a better accuracy than the one obtained with FR4.

B. Discussion and Analysis of the Results

In this section, the line losses α_{Typ} (dB/m) considering a typical microstrip line of width $w = 3$ mm over a $h = 1.6$ mm height substrate, are compared for all materials.

1) Interface Material: The interface material was applied in a previous work to polycotton to smooth its surface and make it ready for silver screen printing of conductive layers [12]. This strengthens the adherence of the conductive layer (especially when the antenna is bent) and reduces surface roughness. The dielectric loss associated with this structure is, however, about 22.4 dB/m, which is high compared to the reference FR4 (7.6 dB/m) and Duroid-5880 (0.3 dB/m). Regarding pure interface material samples, the results show a relative permittivity of 3.26 and a loss tangent of 0.063. These values are slightly higher than those of the polycotton-interface material sandwich ($\varepsilon_r = 3.23$ and tan$\delta = 0.06$). Considering that 2/3 of the thickness of the sandwich is interface material, it is apparent that the interface layer is the main contributor to the high dielectric loss of the structure. Interface materials should therefore be used sparingly, and further researched for lower-loss variants.

2) Woven Fabrics: Cotton and woven polyester fabrics are widely used in garment industry. Both exhibit similar loss tangent values of 0.028. However, the 8.5 dB/m of loss for cotton is higher than the 7.6 dB/m for polyester, as a result of cotton's higher relative permittivity [21]. Both materials appear to be comparable with FR4 (7.6 dB/m), which make them good candidates for a wide range of low-cost RF consumer electronics applications. The surface of woven fabrics is smooth and therefore suitable for screen printing. The weave pattern of fabrics can have an effect on the density of fibers in the fabric which could affect the high-frequency electrical characteristics of the fabric. A systematic characterization of the fabric material of interest is essential in order to achieve an accurate design.

3) Polymers: Kapton has a loss below 5 dB/m. Although the tested sample had a thickness of 1 mm, thin 125-μm flexible kapton is available. Thus, RF circuits and antennas can be designed on thin Kapton and integrated with clothing or any application requiring flexibility, with better performance than FR4 (e.g., STMicroelectronics M24LR04E NFC/RFID flexible tag).

4) Felts: Polyester felt is considered here. It should be noted that felt fabric has a rough and irregular surface which is nonoptimal for screen printing. The relative permittivity of felt is very close to 1 (air) due to its porosity (∼40% air in volume). Polyester felt has a dielectric loss of 5.8 dB/m,

which is better than FR4 (6.7 dB/m). Polyester felt shows lower dissipation than woven polyester primarily due to its higher proportion of air.

We conclude from this paper that polyester felt is the fabric with the lowest loss. Its relatively high nominal thickness (1.65 mm) is an additional advantage to improve antenna's performance such as efficiency and bandwidth [18]. However, due to its porosity, felt is susceptible to compression that could detune the RF circuit or antenna. As Polyester felt is not suitable for silver screen printing, the use of conductive fabric is preferred for the conductive parts of the antenna.

5) Effect of Environmental Conditions: The humidity and temperature do have an effect on the high-frequency parameters of fabric materials, as a proportion of water (depending on the relative humidity level and temperature) is absorbed by the fabric fibers. Detailed studies were performed in [22] and [23]. The increase in relative humidity translates to an increase in the amount of water in the fibers, which increases by consequence the dielectric constant and the loss tangent of the fabric. The variations of temperature have the same effect [23].

One of the conclusions from [22] was that natural fibers are much more sensitive to humidity than synthetic fibers. The materials selected for the design of the present harvester are synthetic, which makes them more immune to variations in environmental conditions.

The experiments in this paper were all realized in an air-conditioned laboratory environment. However, no precise record was made of temperature and humidity levels. The accurate quantification of the effect of a given relative humidity and temperature level requires a dedicated study and is outside the scope of this paper.

III. Antenna Design

Patch antenna with ground plane is very suitable for the realization of fabric wearable antennas. Also, a full ground plane has been shown to reduce the specific absorption rate value by a factor of 3 when compared to an antenna without ground plane [24]. Furthermore, a ground plane results in a thinner overall system when compared to other shielding options, such as air or fabric spacing gaps [25], electromagnetic band gap [26], and artificial magnetic conductor [27]. In this paper, a planar multilayer-fabric patch antenna is chosen with proximity-coupled feed [28].

The study in Section II suggested the use of polyester felt and woven polyester for their reduced loss. Early design simulation (using ADS Momentum with pure copper as the conductive material) showed that two layers of polyester felt and one layer of woven polyester achieve a radiation efficiency above 70%. This 3.7-mm multilayer structure also improves the bandwidth, which makes the antenna more robust when bent or worn. The thin 0.33-mm woven polyester is interlaced between the polyester felt fabrics and will be used later as a dielectric for the broadside coupling with the rectifier. A flexible conductive fabric (80-μm-thick woven copper-plated polyester fiber fabric, from LessEMF Inc. with 0.18 Ω/sq at 2.45 GHz [8]) is used for the patch, the feed line, and the ground plane. An adhesive spray (3M Display Mount) was used for mechanical bonding between the various

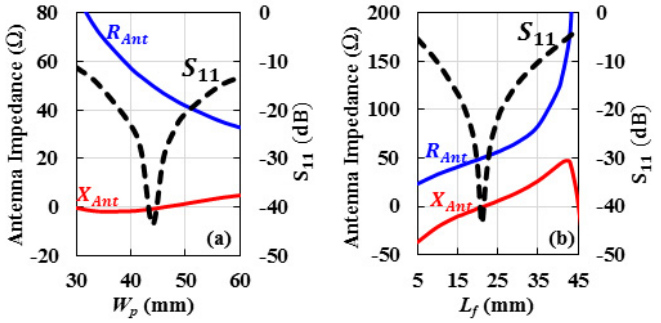

Fig. 6. Simulated antenna impedance, $Z_{\text{Ant}} = R_{\text{Ant}} + j \times X_{\text{Ant}}$, and input response S_{11} as function of the patch width W_p, and the length of the microstrip feed line L_f. (a) Variation of W_p with constant $L_f = 21$ mm. (b) Variation of L_f with constant $W_p = 44$ mm. The impedance of the antenna is calculated 10 mm from the edge of the patch in the x-axis direction, as shown in Fig. 7.

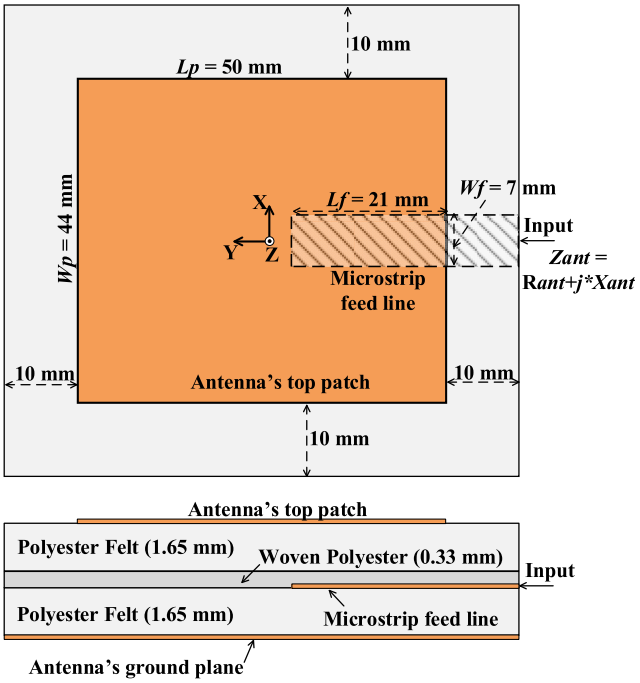

Fig. 7. Layout of the all-fabric antenna. All conductive parts are made from flexible copper fabric.

fabric layers. As only a small quantity of adhesive is required, no degradation of the flexibility was noticed.

The antenna in Fig. 7 was optimized using ADS Momentum. The length of the patch resonant at 2.45 GHz is $L_p = 50$ mm and its width W_p was optimized to achieve a good 50-Ω match [see Fig. 6(a)]. The width of the 50-Ω microstrip feed line is $W_f = 7$ mm, its length L_f impacts both the antenna's resistance and reactance [see Fig. 6(b)]. The final design and the optimized parameters are given, as shown in Fig. 7 and a photograph of a fabricated prototype is shown in Fig. 8. The ground plane extends 10 mm beyond the patch edges in order to improve the isolation from the immediate environment.

IV. Fabric-to-Rigid PCB Interface Design

Establishing an RF connection between fabric and a rigid PCB is one of the main sources of failure in smart electronic

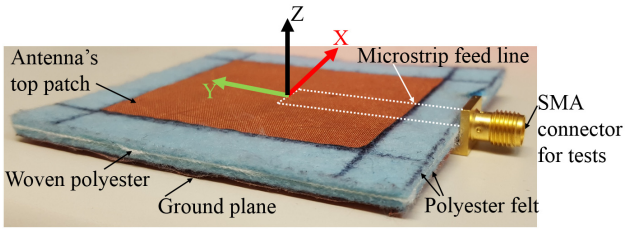

Fig. 8. Fabricated prototype of the all-fabric antenna.

textile applications [29]. Specifically, at RF where insertion loss and stability of the interconnection are of most important. In order to avoid the use of fragile coaxial cable connection, metallic snap-on buttons have been proposed with a working frequency range up to 5 GHz and insertion loss better than 0.8 dB [13]. Similarly, conductive hook and loop fastener was proposed in [30] with insertion loss about 1 dB at 4 GHz. Both techniques can be used to allow the user to unmount the electronic module from the fabric if needed.

A nongalvanic interconnection was proposed in [31] using magnetic coupling between two coils, one on fabric and the other on a flexible PCB. The drawback of that proposed system is related to the inherent complex impedance of the transformer at both terminals, i.e., fabric and PCB, which reduces the operational bandwidth of the transition according to the Bode–Fano Criterion [21]. An additional drawback is the noncompatibility with a 50-Ω standard connection, making experimental tests more challenging.

We present herein two techniques that are expected to perform better in term of bandwidth and 50 Ω compatibility: slot-coupled microstrip lines and broadside-coupled (or stacked) microstrip lines [21]. Both techniques are convenient and easy to implement in this type of application and are well-known to the microwave community. The novelty therefore is the combination of fabric and rigid material.

Slot-coupled microstrip line is a better option if the PCB is to be placed back-to-back with the fabric antenna. In order to preserve the flexibility of the antenna, the microstrip line feeding the antenna must be slot-coupled to the second microstrip line on PCB at the extremity of the antenna. This implementation is different from an aperture-fed antenna, in which case the PCB is to be placed at the back-center of the antenna, which reduces its flexibility. Using this technique, the operational bandwidth can be made very large using a multiresonant slotline resonator [32].

Broadside-coupled microstrip line is a better option if the PCB and the antenna face the same direction, which is the case in our application since the rectifier uses microstrip lines. Here a series capacitive coupling is created between the two microstrip lines. Its effect on the impedance of the line can be minimized by improving the coupling, i.e., increasing the equivalent capacitance. This way, the impedance at both input and output terminals stays mainly real, leading to an improvement of the matching bandwidth.

Full-wave electromagnetic simulation using ADS Momentum is used to optimize the structure proposed in Fig. 9(a). The input is the 50-Ω microstrip line from the antenna. Woven polyester with a nominal thickness h of 0.33 mm is used as

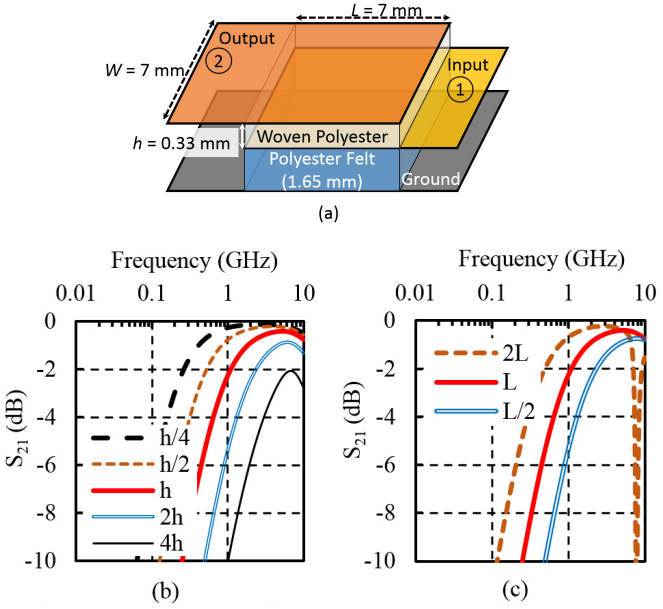

Fig. 9. Simulation of the broadside coupling performance. (a) 3-D view of the broadside-coupled microstrip lines. (b) S_{21} with variable h ($L = 7$ mm). (c) S_{21} with variable L ($h = 0.33$ mm).

a baseline for the broadside coupling. S_{21} is calculated from 10 MHz up to 10 GHz for various values of L and h in order to give a wide overview of the operation bandwidth of the coupling. As shown in Fig. 9, S_{21} is improved with increased coupling area (by increasing L) and with reduced thickness due to the increase in the equivalent capacitance.

We define the bandwidth for an insertion loss of 1 dB. For a thickness h (0.33 mm), the bandwidth extends from 1.8 GHz up to over 10 GHz. More improvement regarding the bandwidth can be mainly achieved by reducing the thickness h. A larger bandwidth from 850 MHz to over 10 GHz is achieved with $h/2$ (175 μm), and from 400 MHz to over 10 GHz with $h/4$ ($\approx$85 μm), as seen in Fig. 9(b).

The nominal thickness h (0.33 mm) gives an insertion loss of 0.7 dB at 2.45 GHz. This performance is largely sufficient for our application. The parameters shown in Fig. 9(a) are, thus, employed for experimental implementation.

V. Rectifier Design

The most critical part of a wireless power transfer receiver is the rectifier because its efficiency dominates the system efficiency at low power levels. The rectifier efficiency is function of all these: frequency, level of the input power, diode type and rectifier circuit topology, substrate, input matching with the antenna, and output dc load.

The rectifier presented here was optimized to operate at 2.450 GHz. A Duroid-5880 substrate ($\varepsilon_r = 2.2$, $\tan\delta = 0.0009$) was used in order to reduce dielectric loss in the input and output microstrip matching circuit. A Schottky diode (SMS7630 with a very low forward voltage $V_f = 60$ to 120 mV at 0.1 mA) was selected in order to optimize the efficiency around -20 dBm. However, this diode suffers from a considerable reverse leakage ($I_{\text{leak}} = 5$ μA)

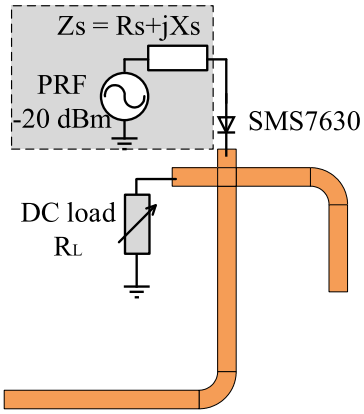

Fig. 10. Harmonic Balance optimization using ADS at −20 dBm input power. For each set of the three variables: Rs, Xs, and R_L, a harmonic balance simulation is run to evaluate the RF/dc efficiency. $R_L = 5$ kΩ, $R_S = 20$ Ω, and $X_S = 260$ Ω are found to maximize the RF/dc efficiency at −20 dBm.

and a very low breakdown voltage ($V_B = 2$ V), which implies that the rectifier efficiency will be reduced at higher power levels. A different diode with lower reverse current and higher V_B (such as HSMS8250 with $I_{\text{leak}} = 3$ μA and $V_B = 3.8$ V) would perform better when the power is above about −15 dBm, as seen in [33].

The input and output matching circuit was designed using ADS and Momentum following this procedure.

1) Two parallel-connected open-circuit quarter-wave stubs were designed using Momentum at the first (2.45 GHz) and second (4.9 GHz) harmonics. The stubs act as a short circuit at their design frequency, providing a low loss return path for the harmonics generated by the diode and thereby improving the rectifier efficiency. The stubs also prevent the harmonics from propagating to the output dc terminal. Simulation showed that the presence of the second-harmonic stub improves the rectifier efficiency by about 1% compared to a single stub configuration. Both stubs are bent in order to occupy the smallest area on the board.
2) As stated above, the rectifier efficiency depends on the input matching to the antenna and on the output load. A co-simulation in ADS is realized, in which the diode is connected to the EM model of the dual-stub filter (see Fig. 10). The stub is loaded with a resistive load (R_L) and the diode is fed by a −20 dBm RF source with variable complex impedance$Z_S = R_S + j * X_S$. A harmonic balance simulation (large signal simulation) is run with simultaneous 3-variable sweep on R_S, X_S and R_L. The optimization gave the following parameters: $R_L = 5$ kΩ, $R_S = 20$ Ω, and $X_S = 260$ Ω.
3) A multilayer structure including fabric layers and a 1.57-mm Duroid-5880 layer is constructed in Momentum, as depicted in Fig. 11. The parameters for the broadside coupling are those found in the previous optimization. Two vias (made from a 0.3-mm radius metallic wire) are used to connect the ground plane of the antenna on fabric to the ground plane of the rectifier. These vias do not need to be flexible as they are connected to the rigid PCB of the rectifier. The electromagnetic waves in the rectifier circuit are confined inside the low loss Duroid-5880 substrate, resulting in an improved rectification efficiency. An L-network microstrip matching is used to transform the antenna's 50-Ω impedance to the diode's optimal complex input impedance. The width of microstrip matching line is gradually reduced in order to reach the required highly inductive impedance while minimizing the effect on the input 50-Ω matching. The layout of the proposed rectifier is depicted in Fig. 11 and a photograph of a fabricated prototype is shown in Fig. 12.

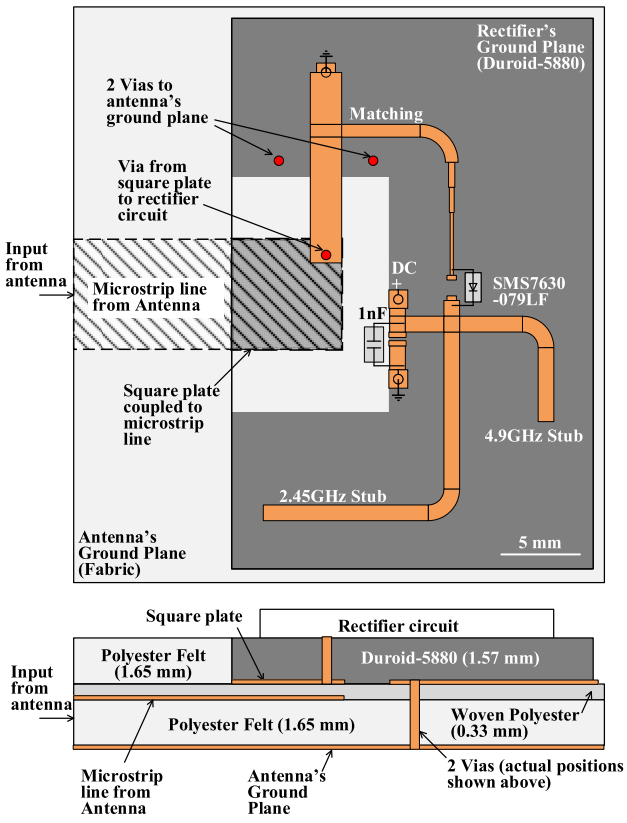

Fig. 11. Layout of the rectifier on Duroid-5880 (35 × 23 mm) including the fabric-to-PCB coupling interface (top view is to scale). All vias are constructed from 0.3-mm radius metallic wire.

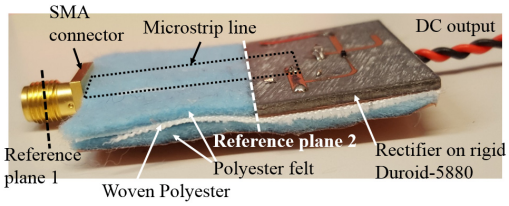

Fig. 12. Fabricated prototype of the rectifier on Duroid-5880 and the fabric-to-PCB coupling interface.

The 50-Ω matching of the antenna and the rectifier facilitates experimental measurement using standard measurement equipment. Eliminating the matching network would not improve the rectifier efficiency considerably as the matching circuit on Duroid-5880 substrate has very low loss. The 50-Ω matching also gives access to a better accuracy when measuring rectifier

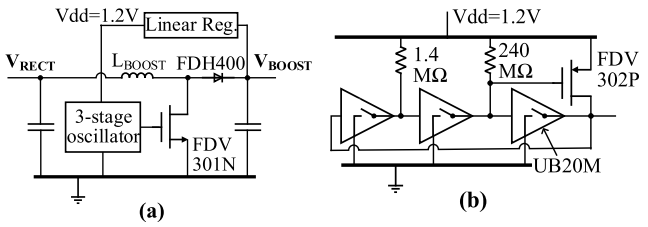

Fig. 13. (a) Self-powered boost converter. (b) MOSFET driver comprising a 3-stage oscillator. The UB20M voltage detector [35] is an ultralow power integrated circuit with an input quiescent current of around 10 pA.

efficiency as the power sources can be calibrated to about 0.1 dB uncertainty. On the other hand, if the rectifier was directly matched to the antenna, radiated measurement in anechoic chamber would have to be used for measuring the efficiency. In that case, the power level received by the rectenna is estimated using a reference antenna connected to a power meter. A typical 0.5 dB uncertainty on the reference antenna gain would dramatically reduce the accuracy of the efficiency measurement.

The vias connecting the ground plane of the antenna to the ground plane of the rectifier can be mechanically supported by a rigid plate at the bottom of the multilayer structure (Fig. 11). If a via is to be used to connect the input microstrip line from the antenna to the rectifier circuit, no mechanical support is possible as the microstrip line is wrapped by fabric layers at both sides, Hence the benefit of the broadside coupling which provides a practical and mechanically robust RF connection.

VI. Power Management Design

Matching the rectenna's output load to the rectenna's optimal impedance $R_{\text{Rect\_optim}}$ is essential in order to maximize rectification efficiency. This is achieved using the power management circuit of Fig. 13. The circuit contains an inductive boost converter that operates in discontinuous conduction mode. In this mode, no feedback control loop is required as the output voltage depends only on the output load. On the other hand, the input impedance of the boost converter in this mode of operation is given by [34]

$$R_{\text{Boost\_in}} = \frac{2L_{\text{Boost}}F_{\text{Sw}}}{\delta^2}\left(1-\frac{V_{\text{Rect}}}{V_{\text{Boost}}}\right) \tag{1}$$

where $L_{\text{Boost}} = 8.1$ mH is the inductance of the boost converter, F_{Sw} is the switching frequency, and δ the duty ratio of the oscillator that drives the MOSFET. Here V_{Boost} is relatively high compared to V_{Rect} (ratio of 26 at -20 dBm RF power), so only the first term in (1) remains, i.e., $R_{\text{Boost\_in}}$ will only depend on L_{Boost}, F_{Sw}, and δ

$$R_{\text{Boost\_in}} \approx \frac{2L_{\text{Boost}}F_{\text{Sw}}}{\delta^2}. \tag{2}$$

The oscillator controlling the boost converter is a ring oscillator, comprising a cascade of three inverters. Each inverter uses the UB20M voltage detector chip developed at the University of Bristol. As shown in the datasheet [35] the open-drain output is activated when the input is close to the detection threshold of about 600 mV. The current consumption is only few picoamperes. The oscillator switches at $F_{\text{Sw}} = 200$ Hz with $\delta = 2\%$, and draws 64 nA from a 1.2-V supply. A low power linear regulator (ZSPM4141 with 20-nA quiescent current) is used to power the oscillator from the output of the boost converter V_{Boost}; the total quiescent current, including that of the regulator, is about $I_{\text{Quiescent\_Boost}} = 150$ nA with $V_{\text{Boost}} = 3$V. The output of the boost converter is connected to a precision source/measure unit (Keysight B2911A) configured as a voltage source. This device allows us to accurately measure the output current and evaluate the converter efficiency. If a storage capacitor (or supercapacitor) is to be used at the output of the boost converter, it should be precharged to about 2 V to kick-start the operation of the boost converter.

It should be noted that the actual optimal parameters of the boost converter ($F_{\text{Sw}} = 200$ Hz, $\delta = 2\%$, and $L_{\text{Boost}} = 8.1$ mH) do not satisfy (2) for $R_{\text{Boost\_in}} = 4$ kΩ as a result of the internal loss of the boost converter not being considered in the derivation of (2). The value of L_{Boost} was experimentally fine-tuned with the boost converter being connected to the rectenna in order to achieve the required optimal impedance $R_{\text{Boost\_in}} = 4$ kΩ.

The matching efficiency η_{Matching} is defined here as

$$\eta_{\text{Matching}} = \frac{\eta_{\text{rect}}(R_{\text{Boost\_in}})}{\eta_{\text{rect}}(R_{\text{Rect\_optim}})} \tag{3}$$

which is the ratio between actual and maximum achievable rectifier efficiency, when the boost converter provides perfect impedance matching.

VII. Experimental Results

A. Patch Antenna Measurement

Simulated and measured input responses S_{11} for the fabric antenna are provided in Fig. 14. The antenna works well at the intended frequency band. This is supposed to be 2 MHz around 2.45 GHz, because no specific bandwidth is required for the receiving antenna harvesting a single tone continuous wave signal (black rectangle in Fig. 14). The measured S_{11} matches well the simulation, with a shift of about 10 MHz in the resonant frequency, which may be due to the connector not modeled and the fabrication tolerances. These can be expected to be below 0.5 mm, resulting in a maximum possible frequency shift of about 25 MHz.

The antenna was tested with tight bending radii in the E- and H-planes [see Fig. 14(a) and (b)]. Contrary to what was reported in [36], the bending in the E-plane [bending axis parallel to W_p, as illustrated in Fig. 15(a)] has negligible effect whereas the bending in the H-plane [bending axis parallel to L_p, as illustrated in Fig. 15(b)] shifts the resonant frequency up. A similar result was reported in [37] where antenna layers were bonded by sewing. In the present antenna, the antenna's substrate fabric layers were bonded using hand-applied spray adhesive. The irregularity of the adhesive spread and the compressible nature of the felt fabric creates a substrate with unpredictable behavior when is deformed; bending the substrate creates some zones with reduced substrate thickness and some zones with increased substrate thickness (compared to

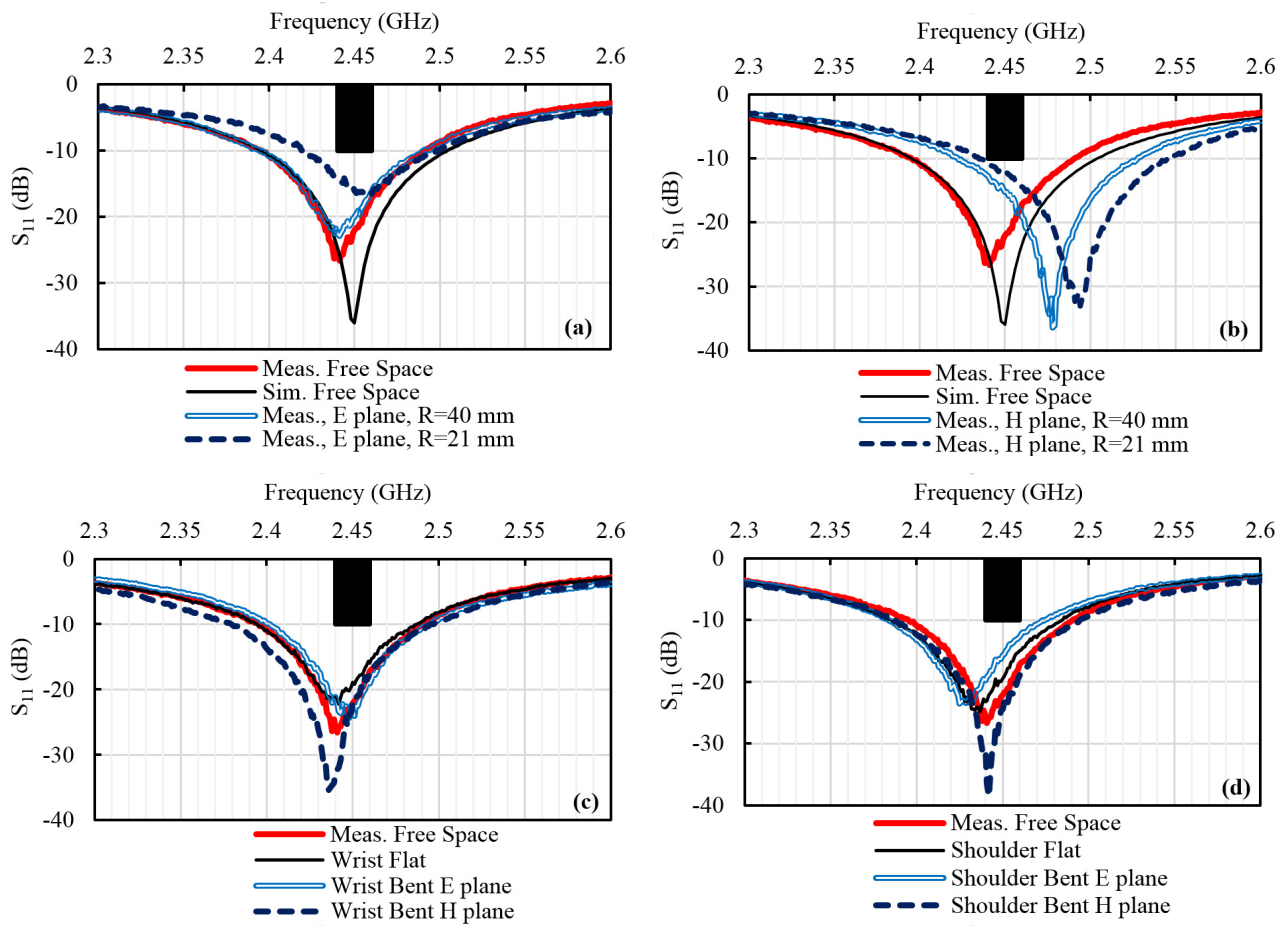

Fig. 14. Measured and simulated S_{11} of the antenna in free space, on body, and with various bending scenarios. (a) Bending in E-plane. (b) Bending in H-plane. (c) Wrist bending. (d) Shoulder bending. The width of the desired operation band is 20 MHz centered at 2.45 GHz with S_{11} below -10 dB (black rectangle).

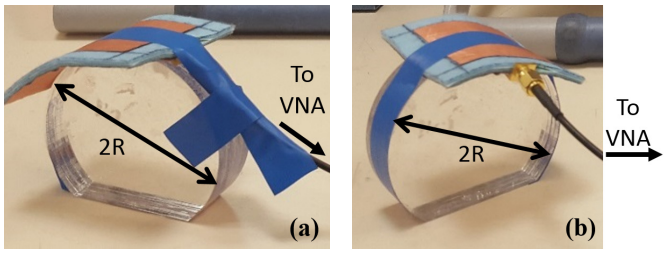

Fig. 15. Experimental setup for E/H bending of the antenna. (a) Bending in the E-plane. (b) Bending in the H-plane.

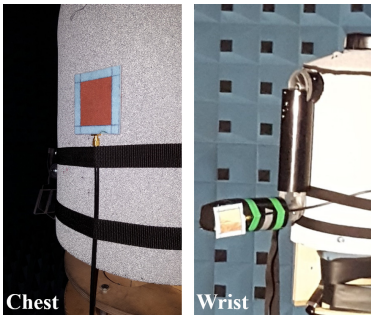

Fig. 16. Fabric antenna mounted on the phantom's body.

the nominal 3.7-mm thickness). Despite these variations, the antenna is robust to bending radii as small as 21 mm. When measured on body, the antenna demonstrates excellent robustness for the various scenarios shown in Fig. 14(c) and (d): wrist, back, flat, and E- and H-planes bending.

Full-3-D radiation pattern measurements were undertaken in the anechoic chamber of the University of Bristol, as depicted in Fig. 16. The efficiency is accurately measured by comparison with a reference monopole antenna following the procedure described in [25]. The antenna was initially mounted on a large ground plane (about 35 $\times$ 35 cm) as a reference best condition scenario, then measured on the chest and the wrist of a human body phantom (see Fig. 16).

It can be seen that the antenna is operating as expected with the cross-polarization component being below about -20 dB for the E- and H-plane patterns [see Fig. 17(a)]. When the antenna is mounted on the phantom's chest and wrist, the pattern appears to be relatively similar to the reference large ground plane's pattern [see Fig. 17(b) and (c)]. The level of back radiation increases because of the relatively small ground plane of the antenna which extends only 10 mm beyond the patch.

A maximum directivity of 9.5 dBi and an efficiency (calculated from measured 3-D radiation pattern) of 73% are

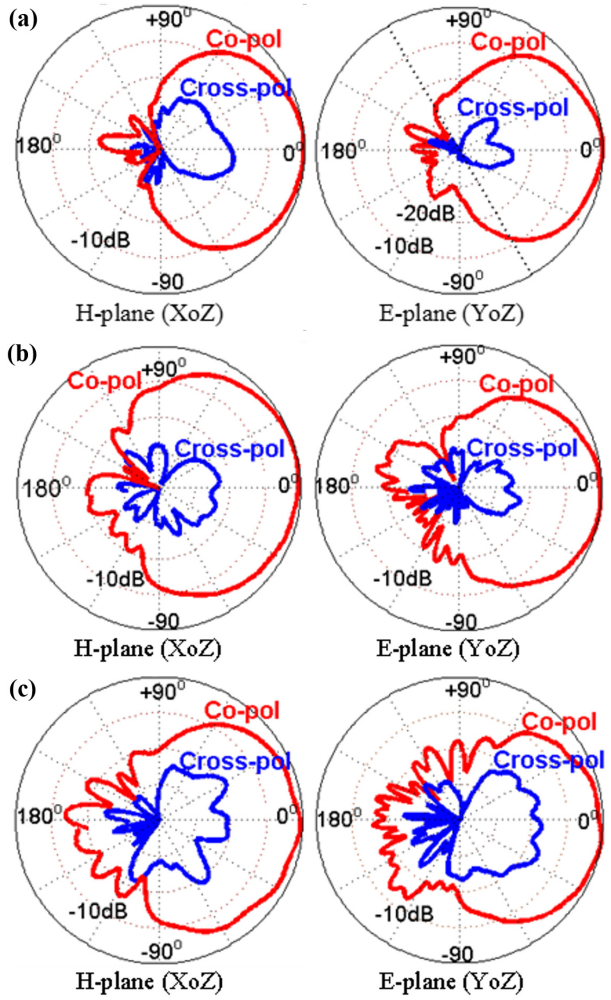

Fig. 17. Measured normalized power radiation pattern of the fabric antenna in various configurations. (a) Large ground plane. (b) Phantom's chest. (c) Phantom's wrist. Scale: 10 dB/div. Range: 0 to −40 dB at center.

TABLE II

MEASURED AND SIMULATED FABRIC ANTENNA'S PERFORMANCE AT 2.45 GHz

	Directivity (dBi)	Gain (dBi)	Efficiency (%)
Simulated (Momentum)	9.0	7.6	73
Measured on large ground plane	9.5	8.1	73
Measured on phantom's chest	9.1	7.3	66
Measured on phantom's wrist	8.9	6.8	62

measured when the antenna is mounted on a large ground plane, which fits well with the simulation (Table II). The maximum gain is indirectly calculated as the product of the measured directivity and efficiency as 8.1 dBi. The gain and the efficiency reduce to 7.3 dBi and 66% on the chest, and to 6.8 dBi and 62% on the wrist.

The proximity of the phantom has little effect on the antenna performance of input response, gain, radiation efficiency, and radiation pattern.

Table III gives an overview of reported fabric antennas, showing their electrical performance as well as their design

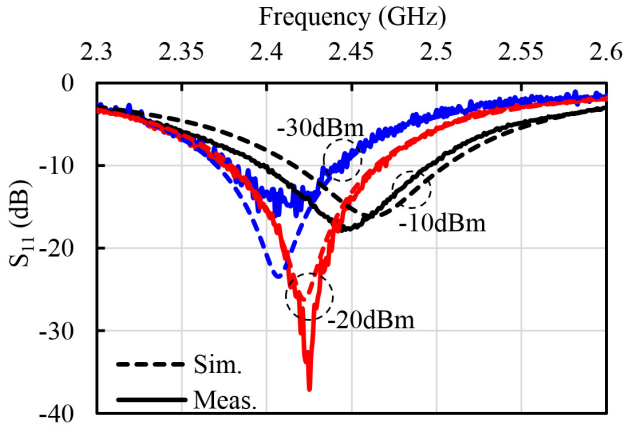

Fig. 18. Measured and simulated rectifier's input response at various power levels.

and construction parameters. Only all-fabric antennas were considered, except Moro *et al.* [8] whose design uses a polymer-based expanded rubber as substrate. The antennas' aperture efficiency ε_{ap} is calculated considering no impedance or polarization mismatch [18]. Also we define the antenna's thickness-normalized aperture efficiency $\varepsilon^*_{\text{ap}}$ as the antenna's aperture efficiency ε_{ap} divided by the antenna's thickness h_a

$$\varepsilon^*_{\text{ap}} = \frac{\varepsilon_{\text{ap}}}{h_a}. \tag{4}$$

This parameter provides a better figure of merit, as it takes into account the thickness of the antenna.

It can be seen that textile antennas in general provide comparable or even better performance than their rigid counterparts (e.g., FR4). In this paper, as the required bandwidth for power transfer is only 2 MHz, the fabric antenna can operate with a bending radius as small as 21 mm in both E- and H-planes. Other reported antennas are designed for communication, and therefore, are required to support a wider bandwidth. For this reason, they are demonstrated with lower curvature. The all-fabric antenna of this paper has the highest on-body measured efficiency of 62%, the highest on-body measured gain of 6.8 dBi, the highest on-body aperture efficiency of 1.3 (considering purely fabric antennas, i.e., excluding [8]), and the highest thickness-normalized aperture efficiency of 0.34.

B. Fabric-PCB Transition and Rectifier Measurement

The rectifier efficiency is measured considering the RF power level at the interface fabric-PCB (reference plan 2 in Fig. 12). An RF power meter was initially used to estimate the RF power at the input of the SMA connector (at reference plane 1 in Fig. 12). Next, the loss in the fabric microstrip line, connecting the two reference planes is deducted (about 0.13 dB estimated using simulation). The measured rectifier efficiency includes, thus, the loss from the interface fabric-PCB.

Measured and simulated S_{11} responses are given in Fig. 18 for various power levels. Measurements are realized using a standard VNA (Rohde & Schwarz ZVL6) where its output

TABLE III
COMPARISON OF THE PROPOSED FABRIC ANTENNA WITH PREVIOUS REPORTED WORK

	This work	Yan et al. 2016 [38]	Moro et al. 2015 [8]	Boyes et al. 2013 [39]	Paul et al. 2013 [25]	Ouyang et al. 2008 [40]
Frequency band (GHz)	Single 2.45 GHz	2.4 GHz ISM	2.4 GHz ISM	1.9-3 GHz	Dual-band 0.5-1 and 1.7-3.6 GHz	Single 2.44 GHz
Antenna type	Patch fed by proximity coupling	Reconfigurable patch	Folded substrate integrated waveguide patch	Slotted broadband PIFA	Planar multiband monopole	Probe-fed patch
Bending radius Bending plane	21 mm E, H	40 mm, E, H [simulated]	50 mm E, H	Not available	Not available	Not available
Efficiency at 2.45 GHz (%) [Measured]	73% [large ground plane] 62 – 66% [on phantom]	38% to 45% [free space]	74% [free space]	75% [free space], 65% [20mm from chest], 50% [on chest]	8% [on phantom] 28% [on RAM]	78% [free space]
Gain at 2.45 GHz (dBi) [Measured]	8.1 [Large ground plane] 6.8 – 7.3 [on phantom]	2 to 3.9 [free space]	5.9 [on-body into jacket]	Not available	Not available	6.6
Body shielding	Ground plane	Ground plane	SIW structure	Ground plane	Layers of felt + EBG	Ground plane
Antenna substrate material	Polyester felt ($\varepsilon_r = 1.2$, $tan\delta = 0.023$), Woven polyester ($\varepsilon_r = 1.5$, $tan\delta = 0.028$)	Felt ($\varepsilon_r = 1.3$, $tan\delta = 0.044$)	Expanded rubber ($\varepsilon_r = 1.45$, $tan\delta = 0.017$)	Felt ($\varepsilon_r = 1.43$, $tan\delta = 0.025$)	Felt ($\varepsilon_r = 1.288$)	Woven polyester ($\varepsilon_r = 1.9$, $tan\delta = 0.0045$)
Conductive fabric (thickness, conductivity at 2.45 GHz)	Woven copper-coated polyester fibre fabric (80 µm, 0.18 Ω/sq [8])	ShieldIt™ conductive fabric (170 µm, 1.18 10^5 S/m)	Woven copper-coated polyester fibre fabric (80 µm, 0.18 Ω/sq)	ShieldIt™ conductive fabric (170 µm, 1.18 10^5 S/m)	Nora-Metalized nylon, (100 µm, 0.03 Ω/sq at dc)	Conductive fabric Satin 5
Mechanical bond	Spray adhesive: 3M® Display Mount™	Not available	Adhesive sheet activated by ironing	Self-adhesive conductive fabric	Not available	Not available
Antenna size (mm)	70 x 64 x 3.7	100 x 100 x 3.3	54 x 54 x 8	50 x 19 x 6	270 x 110 x 1.2	115 x 73 x 4
Aperture efficiency	1.7 [large ground plane] 1.3 - 1.4 [on-body]	0.24 – 0.46 [free space]	2.4 [on-body into jacket]	Not available	Not available	0.94 [free space]
Thickness-normalized aperture efficiency (mm^{-1})	0.46 [large ground plane] 0.34 - 0.4 [on-body]	0.07 - 0.14 [free space]	0.3 [on-body into jacket]	Not available	Not available	0.23 [free space]

Legend: EBG: Electromagnetic Band Gap, **RAM**: Radiation Absorbing Material, **SIW**: Substrate Integrated Waveguide.

power is set to various discrete levels. Simulations were realized using the ADS LSSP simulation module (large-signal S-parameters, also called power-dependent S-parameters) which allows the user to set the power level of the source. The rectifier is well-matched at -20 and -10 dBm (measured $S_{11} < -10$ dB at 2.45 GHz). The rectifier is slightly mismatched at -30 dBm ($S_{11} = -8.5$ dB), as this power level is outside the design range. The input response S_{11} changes with the RF power as a result of nonlinear variations of the complex input impedance of the diode with the RF power. In fact, when the RF power level at the input of the diode changes, the operation point of the diode on its nonlinear I–V curve changes accordingly, leading to a change in the real impedance of the diode. The imaginary part of the impedance change is due to the consequent nonlinear change in the currents and voltages on the parasitic capacitances and inductances around the ideal diode. The resonance shifts to high frequency with increased power level. The simulation fits well to the measurement especially at -20 dBm. Both the antenna and the rectifier are well matched to 50 Ω at the frequency and power levels of interest, which mitigates any matching loss when they are connected. Fig. 19 shows the simulated and measured RF/dc efficiency of the rectifier as function of the frequency. The same nonlinear behavior of the diode makes the matching to shift to higher frequencies with increased power level. At -10 dBm a maximum efficiency

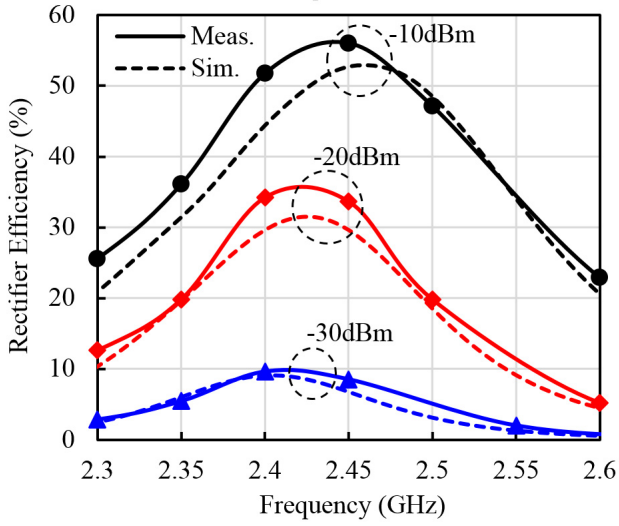

Fig. 19. Measured and simulated rectifier's efficiency at various power levels.

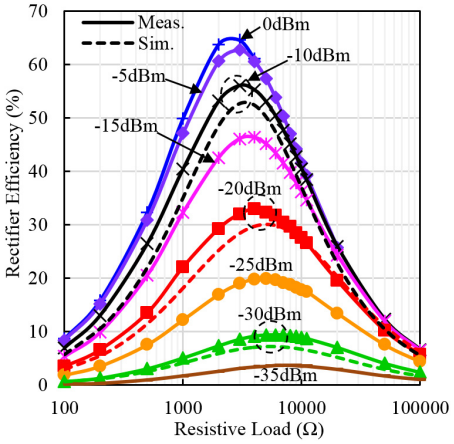

Fig. 20. Measured and simulated rectifier efficiency at 2.45 GHz as function of the resistive load for RF power levels from −35 to 0 dBm.

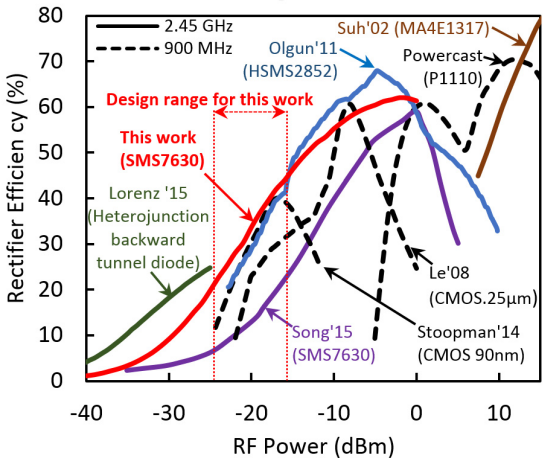

Fig. 21. Rectifier of this paper compared with the state of the art at 2.45 GHz: Lorenz'15 [42], Song'15 [41], Olgun'11 [33], and Suh'02 [44]. Also, integrated circuit implementations for 900 MHz are shown: Powercast [45], Stoopman'14 [43], and Le'08 [46]. The rectifier in this paper is optimized for −20 dBm, where its efficiency of 33.6% is about 17% higher than that of Olgun'11.

of 56% is achieved at 2.45 GHz. At −20 dBm, the efficiency is 33.6% at 2.45 GHz and 34.2% at 2.4 GHz, these values are the highest reported efficiencies at −20 dBm. At −30 dBm, a maximum of 9.6% is obtained at 2.4 GHz.

Fig. 20 shows the measured and simulated rectifier efficiency as function of the resistive load for power levels from −35 to 0 dBm at 2.45 GHz. At each power level, a maximum efficiency is obtained for a given value of the resistive load, this can be considered as the rectenna's optimal load impedance. The optimal impedance $R_{\text{Rect\_optim}}$ is 2.6 kΩ at 0 dBm, 4 kΩ at −20 dBm, and 7.2 kΩ at −35 dBm. The boost converter (Section VI) is designed to match the rectenna at −20 dBm, i.e., to 4 kΩ. As the change in the rectifier's optimal impedance is relatively small, a good matching is expected for a wide range of RF power.

The measured efficiency appears to be slightly higher than the simulated one (Figs. 19 and 20) which could be explained by the fact that the spice model of the diode is limited especially at high power levels above −10 dBm. This limitation also appears in [41]. Also, the efficiency is very sensitive to the source power level accuracy. In fact, a 0.1-dB shift in the source power could change the efficiency by 2%.

Reported measured efficiencies against RF power are plotted in Fig. 21. Solid lines show rectifiers operating at 2.45 GHz, using discrete diodes (see labels in Fig. 21). Dashed lines show integrated rectifiers with the highest reported efficiencies; these operate at 0.9 GHz. Of those using commercially available diodes, the rectifier presented herein has the highest efficiency at power levels below −16 dBm.

The present rectifier has also a wide power operating range, over three orders of magnitude. The maximum efficiency is 64.6%, achieved at 2.45 GHz, −2 dBm RF power level, and with 3-kΩ load. The high efficiency achieved around −20 dBm is a result of the following factors.

1) Use of Duroid-5880 substrate with extremely low dielectric loss.
2) Unlike other systems such as Song'15 [41] in which the rectifier was designed for a wide range of RF power levels, the rectifier of this paper was locally optimized at −20 dBm.
3) The layout of the rectifier was designed carefully in Momentum with: a) optimized close meshing for better accuracy and b) accurate placement of the ports.
4) In the optimization process, finding the optimal input impedance of the diode was realized with a variable load resistance. This way, a better accuracy for the optimal operation point is achieved (Section V).

Lorenz'15 [42] achieves remarkable rectifier efficiencies at extremely low power levels using a custom designed heterojunction backward tunnel diode. Their efficiency is reported to be below that of this paper at −20 dBm. The integrated circuit rectifiers of Fig. 21 are optimized for high sensitivity rather than efficiency. Therefore the rectifier of Stoopman'14 [43] would provide higher open-circuit voltage at −20 dBm than the rectifier in this paper. The design reported by Song'15 [41] is a multiband rectifier with a higher efficiency at frequency bands below 2.45 GHz. However, for the sake of a fair comparison, only their 2.45-GHz results have been plotted here.

At high power levels, about 0 dBm, the efficiency of the present rectifier starts to reduce, as expected, as the dc output voltage approaches the breakdown voltage of the diode. The same phenomenon is present in the other reported Schottky-diode-based designs.

C. Wristband With Parallel- and Series-Connected Rectennas

The RF harvesting wristband of Fig. 2 comprises two rectennas, with a 40-mm curvature radius. The goal is to combine and use them in the most efficient way. The two rectennas can operate in three different ways: operate independently, connected in parallel or connected in series. A baseline performance level is first established without the use of power management circuits, for the case when one rectenna faces the RF power source, while the other one faces in the opposite direction (see Fig. 22). This configuration emulates

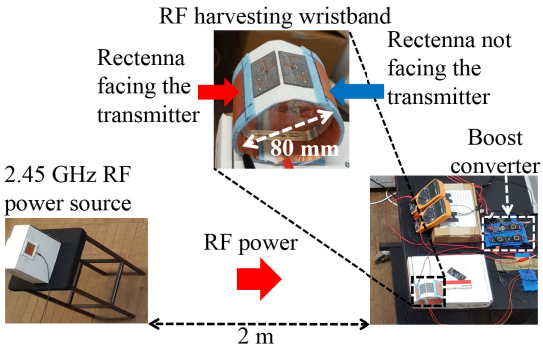

Fig. 22. Measurement setup for the harvesting wristband.

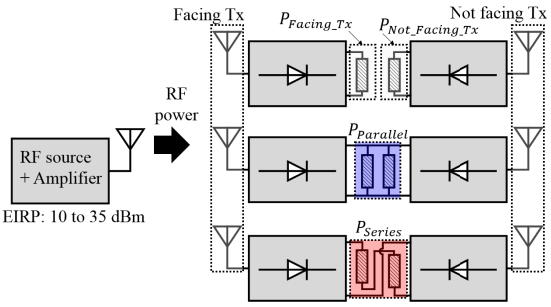

Fig. 23. Measurement setup for testing various rectenna interconnection scenarios for the harvesting wristband: single, parallel, and series. The value of each resistor is 4 kΩ.

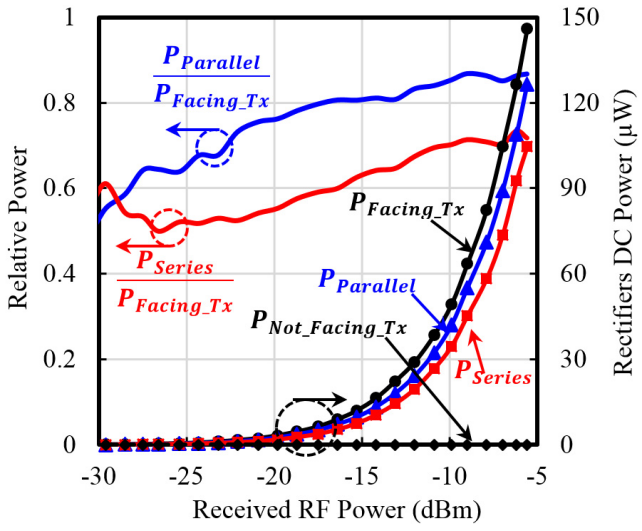

Fig. 24. Measured dc power and relative power in various interconnection scenarios (see Figs. 22 and 23).

a scenario where the wristband is worn by a user. As shown in Fig. 22, due to the curvature of the wristband, the rectennas consequently face opposite directions. The wristband is positioned 2 m away from the transmitter, in a realistic indoor environment. The two rectennas are first measured separately with a 4-kΩ load, and then connected in parallel with a 2-kΩ load and in series with an 8-kΩ load (see Fig. 23). The dc power output against received RF power is shown in Fig. 24, for the two individual rectennas, and for the two combined systems.

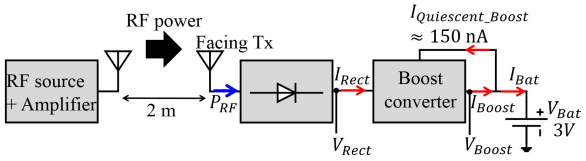

Fig. 25. Experimental setup for the measurement of the complete system. This setup corresponds to one channel where the other channel is identical. For the overall system, the output terminals of the two boost converters are connected in parallel to the output Battery.

The received RF power is the power at the input of the rectifier, measured using a reference calibrated rectenna. This is made from a fabric antenna (identical to the one on the wristband harvester) connected to rectifier with known RF/dc transfer characteristic. A lookup table is used to estimate the RF power level at the input of the rectifier from the output dc voltage of the reference rectenna. Fig. 24 also shows the relative power of each combined system, defined as the total dc output of a system divided by the output of the rectenna facing the transmitter. A relative power of 1 would signify that the rectenna facing away from the transmitter has no impact on the system.

It is apparent, that when the two rectennas are separate, only the rectenna facing the transmitter generates dc power while the other rectenna generates almost no power. When connected in parallel or in series, the relative power is below 1, showing that power is lost due to connecting to the rectenna facing away from the transmitter. Up to 50% of the potential output is seen to be lost, which is a result of voltage reversal in the series connection, and reverse leakage current in the parallel connection [47]. This loss appears in direct-connected systems whenever one rectenna receives less power than the other.

The use of 2 and 8 kΩ as optimal impedances for the series and the parallel configurations, respectively, is an approximation. In fact, it has been verified experimentally that for the parallel unbalanced configuration, the second rectifier not receiving RF power has little impact on the optimal impedance. While for the series configuration, the change in the optimal impedance is more pronounced but does not reach two times the optimal impedance of a single rectenna. This does not affect the fact that a considerable proportion of power is lost in the other rectenna not receiving any RF power. A simple calculation can show that doubling or dividing the optimal impedance of the rectenna by 2 only reduces the output dc power by about 10% (can also be seen in Fig. 20). Therefore, we estimate that the results presented in Fig. 24 are quite accurate.

D. Complete RF Wristband Using Power Management

A power management circuit per rectenna permits the separation of rectenna channels to avoid the loss shown in the previous section, and ensures that each rectenna is working at its maximum power point. For the overall system, two identical channels exist with the output terminals of the two boost converters being connected in parallel. The diagram of one channel is shown in Fig. 25.

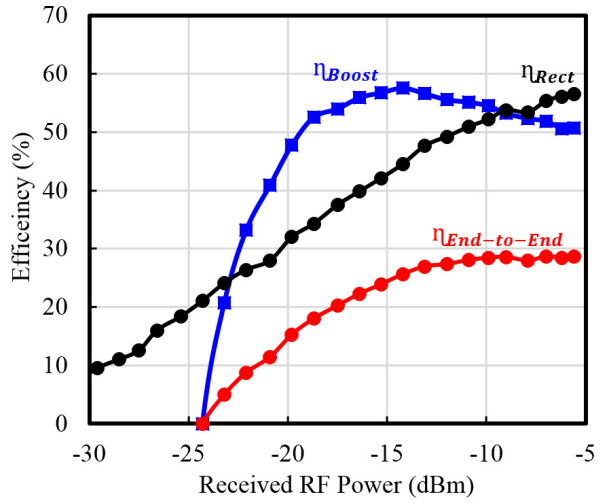

Fig. 26. Measured efficiencies as function of the received RF power. The results shown here correspond to the setup in Fig. 25.

Using the notation of Fig. 25, the rectifier efficiency is

$$\eta_{\text{Rect}} = \frac{P_{\text{Rect}}}{P_{\text{RF}}} = \frac{I_{\text{Rect}} V_{\text{Rect}}}{P_{\text{RF}}} \tag{5}$$

the boost converter efficiency is

$$\eta_{\text{Boost}} = \frac{P_{\text{Boost}} - P_{\text{Quiescent\_Boost}}}{P_{\text{Rect}}} = \frac{I_{\text{Bat}} V_{\text{Bat}}}{I_{\text{Rect}} V_{\text{Rect}}} \tag{6}$$

and the end-to-end efficiency is

$$\eta_{\text{End-to-end}} = \eta_{\text{Rect}} \eta_{\text{Boost}}. \tag{7}$$

Measured rectifier, boost, and end-to-end efficiencies against received RF power are shown in Fig. 26.

The rectifier efficiency increases monotonically with the RF power from 32% at −20 dBm to 56% at −5.6 dBm. This agrees well with the results of Fig. 21, where the rectifier is investigated in isolation. Results are provided up to −5.6 dBm, as the source saturates at this point, although from Fig. 21 it is apparent that the rectifier's efficiency continues to increase. The efficiency of the boost converter is positive from −24.3 dBm and achieves a maximum of around 57% at −14.2 dBm. The end-to-end efficiency reaches a maximum of 28.7% at −7 dBm.

Fig. 27 shows the rectenna's optimal load impedance, the boost converter's input impedance, and the impedance range where the matching efficiency exceeds 95%. The boost converter impedance is seen to provide at least 95% matching over the entire working range, from −24.3up to −5.6 dBm.

Table IV compares the results of this paper, with those of reported low-input-power RF harvesters that comprise a rectenna and an impedance-matching power management circuit. The flexible system developed in this paper has the lowest RF power threshold of −24.3 dBm, and the highest matching efficiency of >95%, despite being the only flexible system. The quiescent consumption of 150 nA achieved in this paper is comparable with the best quiescent current achieved by the integrated design of [48]. The system of [49] achieves a higher end-to-end efficiency, as it is optimized for higher power

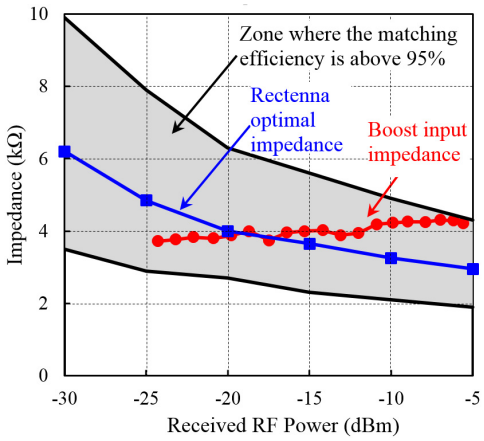

Fig. 27. Measured impedances, and zone where matching efficiency exceeds 95%. This zone is derived from the results of Fig. 20.

TABLE IV
COMPARISON OF LOW-POWER RF HARVESTERS COMPRISING RECTIFIER AND POWER MANAGEMENT CIRCUIT

	This work	Hsieh et al. 2015 [49]	Paing et al. 2011 [48]	Paing et al. 2008 [34]
Frequency	**2.45 GHz**	830 MHz	1.93 GHz	2.4 GHz
Minimum P_{RF}	**-24.3 dBm**	-17 dBm	-13.5 dBm	0 dBm
Maximum end-to-end efficiency	**28.7% at -7 dBm**	44.1% at -12 dBm	10% at 3.3 dBm	16.7% at 4 dBm
Impedance matching efficiency	**>95%**	not available	not available	85 to 92.5%
Controller quiescent consumption	**150 nA at 3V**	1.56 µA at 2 V	200 nA at 1.95 V	4.82 µA at 4.15 V
Antenna	**Flexible**	RF source	Rigid	Rigid

levels and therefore has a higher minimum power threshold and reduced range. The system reported in this paper was optimized for −20 dBm, a power at which none of the reported rigid systems can operate.

VIII. CONCLUSION

This work reports a flexible RF power harvesting system with a minimum RF operating threshold that is 7.3 dB lower than the best reported rigid system.

Several novelties are presented in this paper. Various fabric and flexible materials are characterized at 2.45 GHz using the two-line method and the T-resonator method. Polyester felt and woven polyester are chosen to design a proximity-coupled patch antenna, which demonstrates a radiation efficiency above 62% when measured on a phantom. The location on the phantom has little effect on input response, radiation efficiency and radiation pattern.

This work assumes that the wearable should be thin, flexible, and close to the body. The 64-mm-wide wristband provides a 10-mm ground plane overlap, which is sufficient to minimize the coupling with the body, and the resulting loss. In this case, the textiles with the lowest loss have been selected. For more constrained envelopes, where, due to a reduced antenna ground plane, the coupling with the body is higher, the best overall performance is not necessarily obtained using the lowest loss materials, and thicker structures may be required [39].

The rectifier of this paper is designed on a rigid substrate, and its efficiency exceeds reported efficiencies in its design range of −24 to −16 dBm with 33.6% measured at −20 dBm, and with a maximum of 64.6% at −2 dBm. The rectifier board is connected to the fabric antenna using broadside-coupled microstrip lines, with an insertion loss below 1 dB over a wide frequency band, from 1.8 to over 10 GHz. This contactless connection avoids the risk of fatigue caused by repeated flexing of the circuit and connector.

A self-powered boost converter with 150-nA quiescent consumption is demonstrated to match the rectenna with over 95% matching efficiency across the entire usage range. The complete system is self-contained, and starts harvesting positive power from −24.3 dBm, which is an improvement of 7.3 dB on the best reported rigid system. The maximum end-to-end efficiency is 28.7% at −7 dBm.

The demonstrated wideband and efficient contactless transition from microstrip to microchip, the low minimum operating power, and the high harvesting efficiency, will advance the development of flexible wearables, unobtrusive medical sensing, Internet of Things devices, and complex multisensor garments.

ACKNOWLEDGMENT

The authors would like to thank M. Abdullah and E. Mellios for their kind technical assistance using the anechoic chamber and for providing the phantom. The authors would also like to thank S. Dumanli from Toshiba TREL for providing the polyester felt samples.

REFERENCES

[1] R. R. G. Perron, G. C. Huang, and M. F. Iskander, "Textile electromagnetic coupler for monitoring vital signs and changes in lung water content," *IEEE Antennas Wireless Propag. Lett.*, vol. 14, pp. 151–154, 2015.

[2] K. Koski, A. Vena, L. Sydanheimo, L. Ukkonen, and Y. Rahmat-Samii, "Design and implementation of electro-textile ground planes for wearable UHF RFID patch tag antennas," *IEEE Antennas Wireless Propag. Lett.*, vol. 12, pp. 964–967, 2013.

[3] H. R. Khaleel, "Design and fabrication of compact inkjet printed antennas for integration within flexible and wearable electronics," *IEEE Trans. Compon., Packag., Manuf. Technol.*, vol. 4, no. 10, pp. 1722–1728, Oct. 2014.

[4] C. Hertleer, H. Rogier, L. Vallozzi, and L. V. Langenhove, "A textile antenna for off-body communication integrated into protective clothing for firefighters," *IEEE Trans. Antennas Propag.*, vol. 57, no. 4, pp. 919–925, Apr. 2009.

[5] A. A. Serra, P. Nepa, and G. Manara, "A wearable two-antenna system on a life jacket for Cospas-Sarsat personal locator beacons," *IEEE Trans. Antennas Propag.*, vol. 60, no. 2, pp. 1035–1042, Feb. 2012.

[6] T. Haagenson, S. Noghanian, P. de Leon, and Y. H. Chang, "Textile antennas for spacesuit applications: Design, simulation, manufacturing, and testing of textile patch antennas for spacesuit applications," *IEEE Antennas Propag. Mag.*, vol. 57, no. 4, pp. 64–73, Aug. 2015.

[7] S. J. Cho, Y. H. Jung, and Z. Ma, "X-band compatible flexible microwave inductors and capacitors on plastic substrate," *IEEE J. Electron Devices Soc.*, vol. 3, no. 5, pp. 435–439, Sep. 2015.

[8] R. Moro, S. Agneessens, H. Rogier, A. Dierck, and M. Bozzi, "Textile microwave components in substrate integrated waveguide technology," *IEEE Trans. Microw. Theory Techn.*, vol. 63, no. 2, pp. 422–432, Feb. 2015.

[9] P. Nepa and H. Rogier, "Wearable antennas for off-body radio links at VHF and UHF bands: Challenges, the state of the art, and future trends below 1 GHz," *IEEE Antennas Propag. Mag.*, vol. 57, no. 5, pp. 30–52, Oct. 2015.

[10] J. G. Hester *et al.*, "Additively manufactured nanotechnology and origami-enabled flexible microwave electronics," *Proc. IEEE*, vol. 103, no. 4, pp. 583–606, Apr. 2015.

[11] X. Lin, B. C. Seet, and F. Joseph, "Fine-pitch surface component mounting on screen-printed fabric circuits," *Electron. Lett.*, vol. 52, no. 12, pp. 1032–1034, 2016.

[12] S.-E. Adami, D. Zhu, E. Mellios, B. H. Stark, and S. Beeby, "A 2.45 GHz rectenna screen-printed on polycotton for on-body RF power transfer and harvesting," in *Proc. IEEE Wireless Power Transf. Conf. (WPTC)*, May 2015, pp. 1–4.

[13] S. J. Chen, C. Fumeaux, D. C. Ranasinghe, and T. Kaufmann, "Paired snap-on buttons connections for balanced antennas in wearable systems," *IEEE Antennas Wireless Propag. Lett.*, vol. 14, pp. 1498–1501, 2015.

[14] H. J. Visser, S. Keyrouz, A. Kihshen, and I. Paraschiv, "Optimizing RF energy transport: Channel modelling and transmit antenna and rectenna design," in *Proc. Antennas Propag. Conf. (LAPC)*, Loughborough, U.K., 2012, pp. 1–8.

[15] Cisco Corp. *Cisco Wireless Control System Configuration Guide, Release 3.2-Appendix B-Supported Country Codes [Cisco Wireless Control System]*, accessed on Apr. 12, 2017. [Online]. Available: http://www.cisco.com/c/en/us/td/docs/wireless/wcs/3-2/configuration/guide/wcscfg32/wcscod.html

[16] M.-Q. Lee and S. Nam, "An accurate broadband measurement of substrate dielectric constant," *IEEE Microw. Guided Wave Lett.*, vol. 6, no. 4, pp. 168–170, Apr. 1996.

[17] F. Declercq, H. Rogier, and C. Hertleer, "Permittivity and loss tangent characterization for garment antennas based on a new matrix-pencil two-line method," *IEEE Trans. Antennas Propag.*, vol. 56, no. 8, pp. 2548–2554, Aug. 2008.

[18] C. A. Balanis, *Antenna Theory: Analysis and Design*, 3rd ed. Hoboken, NJ, USA: Wiley, 2005.

[19] K.-P. Lätti, M. Kettunen, J.-P. Ström, and P. Silventoinen, "A review of microstrip T-resonator method in determining the dielectric properties of printed circuit board materials," *IEEE Trans. Instrum. Meas.*, vol. 56, no. 5, pp. 1845–1850, Oct. 2007.

[20] J. M. Heinola, K. P. Latti, P. Silventoinen, J. P. Strom, and M. Kettunen, "A new method to measure dielectric constant and dissipation factor of printed circuit board laminate material in function of temperature and frequency," in *Proc. 9th Int. Symp. Adv. Packag. Mater. Process. Properties Interfaces*, Mar. 2004, pp. 235–240.

[21] D. M. Pozar, *Microwave Engineering*, 4th ed. Hoboken, NJ, USA: Wiley, 2011.

[22] C. Hertleer, A. V. Laere, H. Rogier, and L. V. Langenhove, "Influence of relative humidity on textile antenna performance," *Textile Res. J.*, vol. 80, no. 2, pp. 177–183, Jan. 2010.

[23] J. Lilja, P. Salonen, and P. de Maagt, "Environmental characterization of industrial fabric for softwearantenna," in *Proc. IEEE Antennas Propag. Soc. Int. Symp.*, Jun. 2009, pp. 1–4.

[24] P. J. Soh, G. Vandenbosch, F. H. Wee, A. van den Bosch, M. Martinez-Vazquez, and D. Schreurs, "Specific absorption rate (SAR) evaluation of textile antennas," *IEEE Antennas Propag. Mag.*, vol. 57, no. 2, pp. 229–240, Apr. 2015.

[25] D. L. Paul, H. Giddens, M. G. Paterson, G. S. Hilton, and J. P. McGeehan, "Impact of body and clothing on a wearable textile dual band antenna at digital television and wireless communications bands," *IEEE Trans. Antennas Propag.*, vol. 61, no. 4, pp. 2188–2194, Apr. 2013.

[26] S. Zhu and R. Langley, "Dual-band wearable textile antenna on an EBG substrate," *IEEE Trans. Antennas Propag.*, vol. 57, no. 4, pp. 926–935, Apr. 2009.

[27] K. Agarwal, Y. X. Guo, and B. Salam, "Wearable AMC backed near-endfire antenna for on-body communications on Latex substrate," *IEEE Trans. Compon., Packag., Manuf. Technol.*, vol. 6, no. 3, pp. 346–358, Mar. 2016.

[28] L. Inclan-Sanchez, J. L. Vazquez-Roy, and E. Rajo-Iglesias, "Proximity coupled microstrip patch antenna with reduced harmonic radiation," *IEEE Trans. Antennas Propag.*, vol. 57, no. 1, pp. 27–32, Jan. 2009.

[29] E. R. Post, M. Orth, P. R. Russo, and N. Gershenfeld, "E-broidery: Design and fabrication of textile-based computing," *IBM Syst. J.*, vol. 39, nos. 3–4, pp. 840–860, 2000.

[30] R. D. Seager, A. Chauraya, S. Zhang, W. Whittow, and Y. Vardaxoglou, "Flexible radio frequency connectors for textile electronics," *Electron. Lett.*, vol. 49, no. 22, pp. 1371–1373, Oct. 2013.

[31] M. Virili, H. Rogier, F. Alimenti, P. Mezzanotte, and L. Roselli, "Wearable textile antenna magnetically coupled to flexible active electronic circuits," *IEEE Antennas Wireless Propag. Lett.*, vol. 13, pp. 209–212, 2014.

[32] X. Guo, L. Zhu, J. Wang, and W. Wu, "Wideband microstrip-to-microstrip vertical transitions via multiresonant modes in a slotline resonator," *IEEE Trans. Microw. Theory Techn.*, vol. 63, no. 6, pp. 1902–1909, Jun. 2015.
[33] U. Olgun, C. C. Chen, and J. L. Volakis, "Investigation of rectenna array configurations for enhanced RF power harvesting," *IEEE Antennas Wireless Propag. Lett.*, vol. 10, pp. 262–265, 2011.
[34] T. Paing, J. Shin, R. Zane, and Z. Popovic, "Resistor emulation approach to low-power RF energy harvesting," *IEEE Trans. Power Electron.*, vol. 23, no. 3, pp. 1494–1501, May 2008.
[35] G. Yang, C. Zhang, B. Stark, P. Proynov, and S.-E. Adami, "Voltage detector," U.K. Patent Application GB 1 607 304.1, Apr. 27, 2016.
[36] T. Kellomäki, "Analysis of circular polarization of cylindrically bent microstrip antennas," *Int. J. Antennas Propag.*, vol. 2012, 2012, Art. no. 858031, 8 pp.
[37] N. Amaro, C. Mendes, and P. Pinho, "Bending effects on a textile microstrip antenna," in *Proc. IEEE Int. Symp. Antennas Propag. (APSURSI)*, Jul. 2011, pp. 282–285.
[38] S. Yan and G. A. E. Vandenbosch, "Radiation pattern-reconfigurable wearable antenna based on metamaterial structure," *IEEE Antennas Wireless Propag. Lett.*, vol. 15, pp. 1715–1718, 2016, doi: 10.1109/LAWP.2016.2528299.
[39] S. J. Boyes, P. J. Soh, Y. Huang, G. A. E. Vandenbosch, and N. Khiabani, "Measurement and performance of textile antenna efficiency on a human body in a reverberation chamber," *IEEE Trans. Antennas Propag.*, vol. 61, no. 2, pp. 871–881, Feb. 2013.
[40] Y. Ouyang and W. J. Chappell, "High frequency properties of electro-textiles for wearable antenna applications," *IEEE Trans. Antennas Propag.*, vol. 56, no. 2, pp. 381–389, Feb. 2008.
[41] C. Song, Y. Huang, J. Zhou, J. Zhang, S. Yuan, and P. Carter, "A high-efficiency broadband rectenna for ambient wireless energy harvesting," *IEEE Trans. Antennas Propag.*, vol. 63, no. 8, pp. 3486–3495, Aug. 2015.
[42] C. H. P. Lorenz *et al.*, "Breaking the efficiency Barrier for ambient microwave power harvesting with heterojunction backward tunnel diodes," *IEEE Trans. Microw. Theory Techn.*, vol. 63, no. 12, pp. 4544–4555, Dec. 2015.
[43] M. Stoopman, S. Keyrouz, H. J. Visser, K. Philips, and W. A. Serdijn, "Co-design of a CMOS rectifier and small loop antenna for highly sensitive RF energy harvesters," *IEEE J. Solid-State Circuits*, vol. 49, no. 3, pp. 622–634, Mar. 2014.
[44] Y.-H. Suh and K. Chang, "A high-efficiency dual-frequency rectenna for 2.45- and 5.8-GHz wireless power transmission," *IEEE Trans. Microw. Theory Techn.*, vol. 50, no. 7, pp. 1784–1789, Jul. 2002.
[45] *Powercast Corp. P1110*, accessed on Jun. 28, 2016. [Online]. Available: http://www.powercastco.com/
[46] T. Le, K. Mayaram, and T. Fiez, "Efficient far-field radio frequency energy harvesting for passively powered sensor networks," *IEEE J. Solid-State Circuits*, vol. 43, no. 5, pp. 1287–1302, May 2008.
[47] N. Degrenne, V. Marian, C. Vollaire, F. Buret, J. Verdier, and B. Allard, "Voltage reversal in unbalanced rectenna association," *IEEE Antennas Wireless Propag. Lett.*, vol. 11, pp. 941–944, 2012.
[48] T. Paing, E. Falkenstein, R. Zane, and Z. Popovic, "Custom IC for ultralow power RF energy scavenging," *IEEE Trans. Power Electron.*, vol. 26, no. 6, pp. 1620–1626, Jun. 2011.
[49] P. H. Hsieh, C. H. Chou, and T. Chiang, "An RF energy harvester with 44.1% PCE at input available power of −12 dBm," *IEEE Trans. Circuits Syst. I, Reg. Papers*, vol. 62, no. 6, pp. 1528–1537, Jun. 2015.

Salah-Eddine Adami received the engineering Diploma degree in electrical engineering from the National Institute for Applied Sciences, Lyon, France, in 2010, and the Ph.D. degree from the Ecole Centrale de Lyon, Lyon, in 2013.

He has been a Post-Doctoral Researcher with the University of Bristol, Bristol, U.K., since 2013. He is part of the Sphere IRC and part of the Electrical Energy Management Research Group. His current research interests include the development of safe and reliable end-to-end solutions for far-field wireless charging.

Plamen Proynov received the B.Sc. and M.Sc. degrees in automation and control engineering from the University of Varna, Varna, Bulgaria, in 2005 and 2008, respectively, and the Ph.D. degree from the Electrical Energy Management Group, University of Bristol, Bristol, U.K., in 2014.

Since 2014, he has been a Post-Doctoral Research Associate in energy management, harvesting, and wireless power transfer with the Department of Electrical Engineering, University of Bristol. He is currently involved in the SPHERE project, where he is investigating sensor-powered electronics and RF power transfer in healthcare applications. His previous research interests included kinetic energy harvesting and renewable micropower sources. His current research interests include low-power power management, energy harvesting, and wireless sensors.

Geoffrey S. Hilton received the B.Sc. degree from the University of Leeds, Leeds, U.K., in 1984, and the Ph.D. degree from the University of Bristol, Bristol, U.K., in 1993, for research on the design and finite-difference time-domain modeling of printed antenna elements.

He was a Design Engineer with GEC-Marconi. He is currently a Senior Lecturer with the University of Bristol. His current research interests include practical antenna and system design for a variety of communications and radar applications such as ground penetrating radar, performance evaluation of antennas in mobile radio, electrically small elements, active/tuneable elements, and vehicle-mounted conformal antennas.

Guang Yang received the Ph.D. degree from the Bio-inspired VLSI Circuits and Systems Group, Department of Bioengineering, Imperial College London, London, U.K., in 2012.

During 2013–2016, he was a Research Associate with the Electrical Energy Management Group, University of Bristol, Bristol, U.K. His current research interests include auditory (cochlea) modeling and signal processing, speech enhancement and psychophysical evaluation, and low-power analog IC design for biomedical and energy harvesting applications.

Chunhong Zhang was born in Shaanxi, China, in 1986. He received the B.Sc. degree from Xidian University, Xi'an, China, in 2007, the M.Sc. degree from Xiamen University, Xiamen, China, in 2010, and the Ph.D. degree from the Institute of Electronics, Chinese Academy of Science, Beijing, China, in 2013.

His current research interests include analog IC design, mainly on power management ICs.

Dibin Zhu received B.Eng. degree in information and control engineering from Shanghai Jiao Tong University, Shanghai, China, in 2004, and the M.Sc. degree in RF communication systems and Ph.D. degree in electrical and electronic engineering from the University of Southampton, Southampton, U.K., in 2005 and 2009, respectively.

He is currently a Lecturer with the Energy Harvesting Research Group, University of Exeter, Exeter, U.K. His current research interests include energy harvesting from various sources, e.g., vibration, sound, wind, human movement, solar, RF, wireless power transfer, etc., and their applications, as well as advanced materials for energy harvesting applications.

Yi Li received the B.Eng. degree in electronic engineering from the University of Warwick, Coventry, U.K., in 2008, and the M.Sc. degree in microsystem technology and Ph.D. degree in printed smart fabrics from the University of Southampton, Southampton, U.K., in 2009 and 2013, respectively.

He possesses more than three years work experience at the University of Southampton. In addition, he has also focused on various novel functional materials formulation development for printable smart fabrics research, including conductor, semiconductor, PV inks, bioelectrodes, metal oxides, and dielectrics. His current research interests include printed fabric-based antennas, capacitors, transistors, solar cells, speakers, and stimulation electrodes.

Steve P. Beeby received the B.Eng. (Hons.) degree in mechanical engineering from the University of Portsmouth, Portsmouth, U.K., in 1992, and the Ph.D. degree in MEMS resonant sensors from the University of Southampton, Southampton, U.K., in 1998.

He was a Principal or Co-Investigator on an additional 18 projects and has coordinated two European Union research projects. He is currently the Head of the Electronics and Electrical Engineering Research Group. He leads the U.K.'s Energy Harvesting Network. He is currently leading three U.K. funded research projects. He is a Co-Founder of Perpetuum Ltd., a University spin-out based upon vibration energy harvesting formed in 2004, Smart Fabric Inks Ltd., and D4 Technology Ltd. He has co-authored/edited four books including *Energy Harvesting for Autonomous Systems* (Artech House, 2010). He has given 14 invited talks and has over 200 publications and 10 patents. He has an h-Index of 39 with $>$9500 citations. His current research interests include energy harvesting, e-textiles, MEMS, and active printed materials development.

Dr. Beeby was the recipient of two prestigious EPSRC Research Fellowships to investigate the combination of screen-printed active materials with micromachined structures and textiles for energy harvesting and was also awarded a Personal Chair in 2011. He is currently the Chair of the International Steering Committee for the PowerMEMS Conference series.

Ian J. Craddock (M'09–SM'10–F'16) is currently a Full Professor with the University of Bristol, Bristol, U.K., and the Director of the flagship "SPHERE" centre (www.irc-sphere.ac.uk) comprising approximately 100 researchers and clinicians involved in Internet of Things (IoT) technology for health. He has been involved in healthcare technology for 15 years and founded a company that is currently completing trials of a CE-marked breast imaging device based on his research. He is currently a Managing Director with the Telecommunications Research Lab, Toshiba, Bristol, where he is responsible for a portfolio of both internal and collaborative communications, IoT, and smart city research. He has authored over 150 papers and serves on the healthcare strategy board for the U.K.'s largest engineering funder.

Bernard H. Stark received the M.S. degree in electrical engineering from the Swiss Federal Institute of Technology, Zurich, Switzerland, in 1995, and the Ph.D. degree in engineering from Cambridge University, Cambridge, U.K., in 2000.

He was a Junior Research Fellow with St. Hugh's College, Oxford, U.K., and a member of the Control and Power Group, Imperial College, London, U.K. He is currently a Reader in electrical and electronic engineering with the University of Bristol, Bristol, U.K., and a member of the Electrical Energy Management Research Group. His current research interests include renewable power sources and power electronics.